

Correction of image distortions in endoscopic optical coherence tomography based on two-axis scanning MEMS mirrors

Donglin Wang,^{1,2} Peng Liang,² Sean Samuelson,³ Hongzhi Jia,¹ Junshan Ma,^{1,*} and Huikai Xie³

¹Engineering Research Center of Optical Instrument and System, University of Shanghai for Science and Technology, Shanghai 200093, China

²WiO Technology Ltd., Co., Wuxi 214135, Jiangsu, China

³Department of Electrical and Computer Engineering, University of Florida, Gainesville 32611, Florida, USA
junshanma@163.com

Abstract: A two-axis scanning microelectromechanical (MEMS) mirror enables an optical coherence tomography (OCT) system to perform three-dimensional endoscopic imaging due to its fast scan speed and small size. However, the radial scan from the MEMS mirror causes various distortions in OCT images, namely spherical, fan-shaped and keystone distortions. In this paper, a new method is proposed to correct all of three distortions presented in OCT systems based on two-axis MEMS scanning mirrors. The spherical distortion is corrected first by directly manipulating the original spectral interferograms in the phase domain, followed by Fourier transform and three-dimensional geometrical transformation for correcting the other two types of distortions. OCT imaging experiments on a paper with square ink printed arrays and a glass tube filled with milk have been used to validate the proposed method. Distortions in OCT images of flat or curved surfaces can all be effectively removed.

© 2013 Optical Society of America

OCIS codes: (110.4500) Optical coherence tomography; (230.4685) Optical microelectromechanical devices; (100.6890) Three-dimensional image processing.

References and links

1. D. Huang, E. A. Swanson, C. P. Lin, J. S. Schuman, W. G. Stinson, W. Chang, M. R. Hee, T. Flotte, K. Gregory, C. A. Puliafito, and J. G. Fujimoto, "Optical coherence tomography," *Science* **254**(5035), 1178–1181 (1991).
2. A. G. Podoleanu, G. M. Dobre, and D. A. Jackson, "En-face coherence imaging using galvanometer scanner modulation," *Opt. Lett.* **23**(3), 147–149 (1998).
3. M. Pircher, E. Goetzinger, R. Leitgeb, and C. Hitzenberger, "Three dimensional polarization sensitive OCT of human skin in vivo," *Opt. Express* **12**(14), 3236–3244 (2004).
4. P. J. Brosens, "Dynamic mirror distortions in optical scanning," *Appl. Opt.* **11**(12), 2987–2989 (1972).
5. V. Westphal, A. Rollins, S. Radhakrishnan, and J. Izatt, "Correction of geometric and refractive image distortions in optical coherence tomography applying Fermat's principle," *Opt. Express* **10**(9), 397–404 (2002).
6. Y. Pan, H. Xie, and G. K. Fedder, "Endoscopic optical coherence tomography based on a microelectromechanical mirror," *Opt. Lett.* **26**(24), 1966–1968 (2001).
7. W. Jung, D. T. McCormick, J. Zhang, L. Wang, N. C. Tien, and Z. Chen, "Three-Dimensional Endoscopic Optical Coherence Tomography By Use of a Two-Axis Microelectromechanical Scanning Mirror," *Appl. Phys. Lett.* **88**(16), 163901 (2006).
8. M. Hafez, T. Sidler, and R. P. Salathe, "Study of the beam path distortion profiles generated by a two-axis tilt single-mirror laser scanner," *Opt. Eng.* **42**(4), 1048–1057 (2003).
9. A. Podoleanu, I. Charalambous, L. Plesea, A. Dogariu, and R. Rosen, "Correction of distortions in optical coherence tomography imaging of the eye," *Phys. Med. Biol.* **49**(7), 1277–1294 (2004).
10. R. J. Zawadzki, A. R. Fuller, S. S. Choi, D. F. Wiley, B. Hamann, and J. S. Werner, "Correction of motion artifacts and scanning beam distortions in 3D ophthalmic optical coherence tomography imaging," *Proc. SPIE* **6426**, 642607, 642607-11 (2007).
11. S. Ortiz, D. Siedlecki, L. Remon, and S. Marcos, "Optical coherence tomography for quantitative surface topography," *Appl. Opt.* **48**(35), 6708–6715 (2009).
12. S. Ortiz, D. Siedlecki, I. Grulkowski, L. Remon, D. Pascual, M. Wojtkowski, and S. Marcos, "Optical distortion correction in Optical Coherence Tomography for quantitative ocular anterior segment by three-dimensional imaging," *Opt. Express* **18**(3), 2782–2796 (2010).

13. J. M. Hudman and J. O. Miller, "Distortion altering optics for MEMS scanning display system or the like," WIPO Patent 2010030467(2010).
14. S. Samuelson, L. Wu, J. Sun, B. Sorg, and H. Xie, "A 2.8-mm Imaging Probe Based On a High-Fill-Factor MEMS Mirror and Wire-Bonding-Free Packaging for Endoscopic Optical Coherence Tomography," *JMEMS* **21**, 1291–1302 (2012).
15. D. L. Wang, L. L. Fu, X. Wang, Z. J. Gong, S. Samuelson, C. Duan, H. Z. Jia, J. S. Ma, and H. Xie, "Endoscopic swept-source optical coherence tomography based on a two-axis microelectromechanical system mirror," *J. Biomed. Opt.* **18**(8), 086005 (2013).
16. D. L. Wang, L. L. Fu, J. Sun, H. Z. Jia, and H. Xie, "Design Optimization and Implementation of a Miniature Optical Coherence Tomography Probe Based on a MEMS Mirror," *Proc. SPIE* **8191**, 81910M, 81910M-10 (2011).
17. T. S. Lian, "Advances in the Theory of Conjugation for Reflecting Prisms in China," *J. Beijing Inst. Technol.* **1**, 1–12 (1992).
18. M. Frigo and S. G. Johnson, "The design and implementation of FFTW3," *Proc. IEEE* **93**(2), 216–231 (2005).

1. Introduction

Optical coherence tomography (OCT) uses interference signals generated by the backscattered light from a sample and a reference mirror to obtain the structural information of the sample at various depths [1]. Three-dimensional (3D) OCT images can be acquired by using 2D optical scanners. There are mainly two types of reflective optical scanners: a single mirror that can perform two-axis scan, or a pair of orthogonally-oriented single-axis mirrors (e.g., galvanometer mirrors). The two orthogonal mirror configuration is widely used in OCT applications, such as ophthalmology and dermatology [2,3]. Scanning by galvanometers results a fan distortion in OCT images which can be corrected by using mapping approaches which find the coordinate transformations between the raw image data and the actual imaging points [4,5]. However, galvanometers are bulky and not suitable for endoscopic OCT because of the stringent size constraints when used in human body in vivo. Micro-Electro-Mechanical System (MEMS) has the advantages of small size, fast speed and low cost. MEMS based endoscopic OCT has been studied over a decade, in which a single MEMS mirror performs the 2D lateral scan [6,7]. Since an OCT interferogram is encoded with optical path length difference, the OCT image will be distorted by the radial optical scan path from the MEMS mirror [8]. For example, a flat surface will appear curved in the OCT image. This distortion is especially pronounced in endoscopic OCT because of its short working distance. The distortion due to a 2-axis MEMS mirror typically has a fan shape while the distortion generated by galvanometers is shaped as a pincushion. Most distortion correction algorithms are based on a point-to-point mapping method [9–11]. Although this method is universal, it needs a complicated mapping process and can only be applied after the original interferogram data are converted to the structural image [12]. Applying this method to correct scanning distortion will consume a lot of computing resource and can hardly approach real-time display. Besides the above algorithms, physical compensation methods such as adding microwedges can also be used [13], but these methods may not be a good choice for endoscopic imaging due to the limited space available inside the probe.

In this paper, we propose a new method to correct distorted OCT images by directly processing the original interferogram spectral data. It is a more fundamental and simpler method and consumes much less computing resource which is critical for real-time high-resolution image display.

2. Material and methods

2.1 Endoscopic OCT based on 2-axis scanning MEMS mirrors

A typical 2-axis MEMS based endoscopic OCT configuration is shown in Fig. 1. A wavelength-varying narrow-band light generated by a swept source is split via a 2×2 fiber coupler into the reference arm and the MEMS mirror based endoscopic probe. A 3D model of the probe is depicted in Fig. 2(a), which is composed of a mount base, a gradient reflective index (GRIN) lens, a single-mode fiber aligned and assembled with the GRIN lens in a glass sleeve, and a MEMS mirror shown in Fig. 2(b). The MEMS mirror is based on electrothermal actuation and has four pairs of unique dual S-shaped bimorph structures to achieve dual-axis

scan with a linear raster pattern [14]. A visible light is also coupled into the MEMS probe to indicate the scanning location by a 1:99 coupler. After the interference signals are picked up by a balanced photodiode, OCT images can be readily reconstructed through routine OCT data processes including digital filtering, numerical dispersion compensation and fast Fourier transform. However, the reconstructed OCT images may be distorted.

The diameter of the fabricated MEMS probe is 3.5mm [15]. The probe body is made of stainless steel for biocompatibility and robustness. In this probe, the GRIN lens is 1mm in diameter and 4.6mm long, and it is cut with 8 degree at both ends to minimize back reflection and eliminate artifacts in OCT images. The light through the lens is focused at 6.5mm. A MEMS mirror chip is located at 2.7mm after the lens. The chip size is 1.6mm \times 1.4mm, and the active mirror plate is 0.8mm \times 0.8mm. A glass window is used to allow the light to pass, and the distance between the MEMS mirror center and the glass window is 1.8 mm, resulting in a 2mm working distance out of the optical window. It has been shown that a flat optical window leads to much smaller light spot distortion and significantly reduced astigmatism, compared to a cylindrical tube which inevitably stretches the light spot in the transverse direction of the tube [16]. An example OCT image obtained by using this probe is shown in Fig. 2(c).

Due to the radial scan of the 2-axis mirror, the optical path lengths are different when the light is directed to various points on a flat surface. As shown in Fig. 2(d), the optical path length in the direction (i,j) is longer than that in the central scan direction (0,0), where i and j stand for the i^{th} and j^{th} pixel in the two orthogonal scan directions. If the reference arm is not shifted to compensate the optical path length differences at different scan angles, it will lead to a curved OCT image for a straight line. For example, as shown in Fig. 2(e), the flat interfaces in a multilayer glass stack all appear curved in the uncorrected OCT image. Without distortion compensation, it will provide false information and degrade the accuracy of the quantitative assessment. Figure 2(f) is the image after distortion corrected.

In this probe design, the MEMS mirror is placed after the GRIN lens. Alternatively the MEMS mirror can be located before the GRIN lens. The main drawback of the latter design is that part of the optical beam will not reach to the GRIN lens even at small scan angles by the MEMS mirror. This is because the GRIN lens is limited to small diameter for endoscopes. The 3.5mm probe is bigger than the biopsy channel of most endoscopes, but it can fit into oral cavity, otorhinolaryngology, proctoscopes and so on. This probe size of probe is selected just for our algorithm validation and smaller probes with diameters less than 2.7mm can be achieved in the near future.

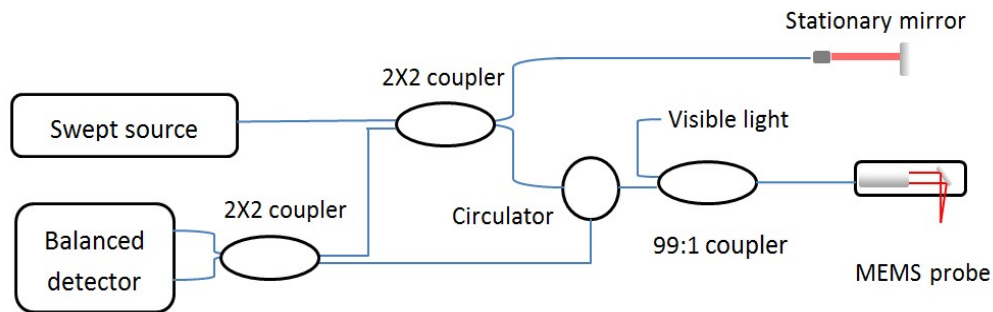


Fig. 1. 2-axis MEMS mirror based endoscopic OCT.

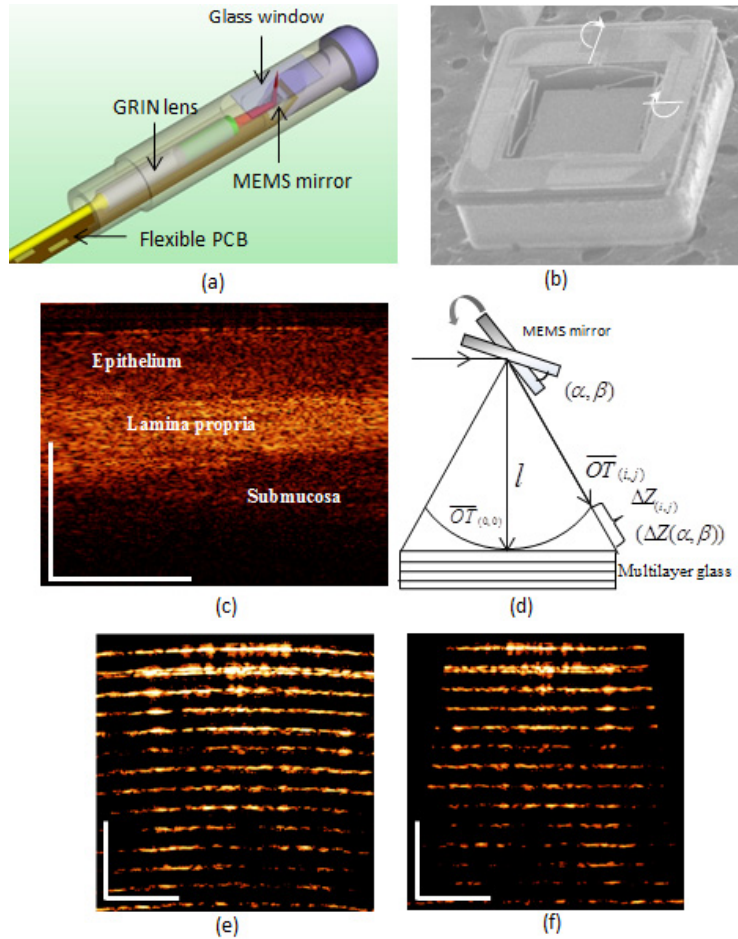


Fig. 2. (a) Endoscope probe; (b) MEMS mirror; (c) OCT image of buccal mucosa by the probe; (d) Different optical path lengths at different scan angles; and (e) OCT image of a multilayer glass; (f) Distortion corrected OCT image of the multilayer glass. White scale bar represents 1mm

2.2 Distortion analysis and modeling

Ray tracing of geometrical optics is utilized to analyze the origin of the scan distortion in OCT images. Figure 3 is an illustration of an optical scanner used in the MEMS based endoscopic probe. It is a ray tracing result by CODE V. The GRIN lens focuses the incident light \overline{LO} in the X direction to the MEMS mirror which is placed at an angle of γ to the X direction. One of the rotation axes of the MEMS mirror is the Y axis, and the other orthogonal rotation axis is denoted as the A axis.

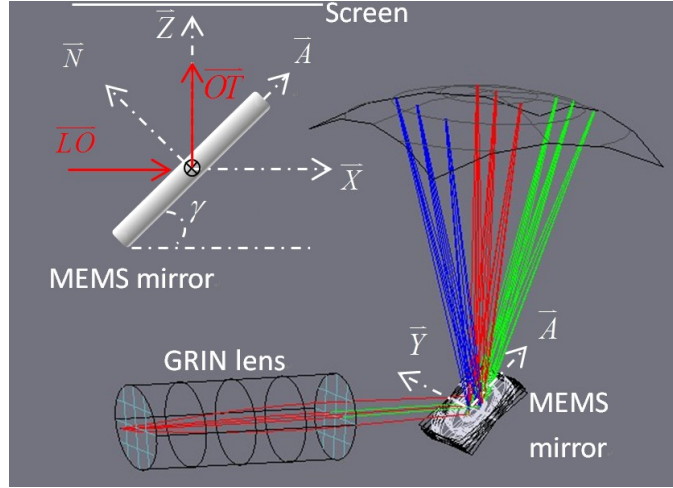


Fig. 3. Schematic of a 2-axis MEMS mirror scanner.

When the MEMS mirror rotates about the Y and A axes, the reflected light \overline{OT} will generate a raster scan pattern on the screen. \overline{OT} is a vector indicating the direction of the scanning beam. For a rotational mirror system, \overline{OT} is given by [17]:

$$\overline{OT}(\alpha, \beta) = [S_A(\beta) \cdot S_Y(\alpha)] \cdot R \cdot [S_A(\beta) \cdot S_Y(\alpha)]^{-1} \cdot \overline{LO} \quad (1)$$

where R and S are the reflection matrix and rotation matrix, respectively, and α and β are the scan angles about the Y and A axes. If the vector N is designated as the normal of the mirror surface plane, i.e., the Y-A plane, then the reflection matrix R can be expressed as:

$$R = \begin{bmatrix} 1 - 2N_x^2 & -2N_x \cdot N_y & -2N_x \cdot N_z \\ -2N_x \cdot N_y & 1 - 2N_y^2 & -2N_y \cdot N_z \\ -2N_x \cdot N_z & -2N_y \cdot N_z & 1 - 2N_z^2 \end{bmatrix} \quad (2)$$

where $\overline{N} = [N_x, N_y, N_z] = [-\sin(\gamma), 0, \cos(\gamma)]$ since vector N is in the X-Z plane. N_x , N_y , and N_z are the x, y, and z components of vector N respectively. If the mirror rotates an angle of θ about a fixed axis P, the rotation matrix $S_P(\theta)$, is given by:

$$S_P(\theta) = \begin{bmatrix} \cos \theta + 2P_x^2 \sin^2 \frac{\theta}{2} & -P_z \cdot \sin \theta + 2P_x P_y \sin^2 \frac{\theta}{2} & P_y \cdot \sin \theta + 2P_x P_z \sin^2 \frac{\theta}{2} \\ P_z \cdot \sin \theta + 2P_x P_y \sin^2 \frac{\theta}{2} & \cos \theta + 2P_y^2 \sin^2 \frac{\theta}{2} & -P_x \cdot \sin \theta + 2P_y P_z \sin^2 \frac{\theta}{2} \\ -P_y \cdot \sin \theta + 2P_x P_z \sin^2 \frac{\theta}{2} & P_x \cdot \sin \theta + 2P_y P_z \sin^2 \frac{\theta}{2} & \cos \theta + 2P_z^2 \sin^2 \frac{\theta}{2} \end{bmatrix} \quad (3)$$

where P_x , P_y , and P_z are the x, y and z components of the vector P. For the above equation, P can be either A or Y, and $\theta = \beta$ for the A axis and $\theta = \alpha$ for the Y axis. For example, when the mirror rotates about the A axis, the left-hand side of Eq. (3) becomes $S_A(\beta)$ and the first term in the matrix on the right-hand side becomes $\cos(\beta) + 2A_x^2 \sin^2(\beta/2)$, where A_x is the x-component of vector \overline{A} and $\overline{A} = [\cos(\gamma), 0, \sin(\gamma)]$. Similarly, when the mirror rotates about

the Y axis, the left-hand side of Eq. (3) becomes $S_y(\alpha)$ and the first term in the matrix on the right-hand side becomes $\cos(\alpha) + 2Y_x^2 \sin^2(\alpha/2)$, where Y_x is the x-component of vector \vec{Y} and $\vec{Y} = [0, 1, 0]$. Assuming the distance between the MEMS mirror center and the focal point of the output light beam is d (d is typically about 2-8 mm for the system shown in Fig. 2(a)), the input light vector \vec{LO} is represented as $\vec{LO} = [d, 0, 0]$. Once the values of all these parameters are specified, the output vector \vec{OT} can be calculated by substituting Eqs. (2) and (3) into Eq. (1). In the following analysis, \vec{OT}' and \vec{OT}'' are used to respectively represent the output light vectors ending at the sample surface and the plane corresponding to the maximum imaging depth. They can be calculated using Eq. (1) by setting d properly.

In the MEMS based endoscopic probe used in this study, the fast scan and slow scan are generated about the Y-axis and the A-axis, respectively, by a pair of low voltage driving signals. The voltage signals applied are triangular waveforms varying from 0 to 4V, which corresponds to the linear angular scan range of the MEMS mirror. The maximum values of α and β both are 8° . Taking the parameters of this probe design, the output vector \vec{OT} is calculated and the results are plotted in Fig. 4. If no correction algorithm is applied in the image processing, distorted OCT images will be generated in Cartesian coordinates. Figure 4(a) shows the scan pattern in the focal plane which is spherical. This phenomenon is denoted as spherical distortion in this paper. It should be noted that this spherical distortion is different from the spherical aberration which is caused by imaging lenses. Even after the spherical distortion is corrected, there still exist residual distortions in reconstructed 3D OCT images. Figure 4(b) shows the top view of the aplanatic focal plane which looks like a fan, namely fan-shaped distortion. In addition, the imaging area is not uniform and keeps increasing along the light propagation direction, as shown in Fig. 4(c), which is denoted as keystone distortion.

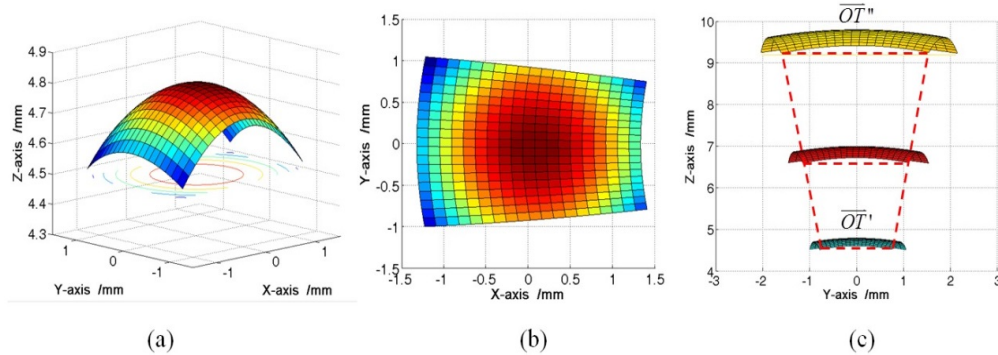


Fig. 4. (a) Aplanatic surface of two-axis MEMS mirror scan in the space; (b) fan-shaped distortion; and (c) keystone distortion.

2.3 Correction method for distorted OCT images

Assume the OCT system records $2L \times M \times N$ matrix data from data acquisition card for 3D image reconstruction, where $2L$ is the number of the axial scans (A-scans), M is the number of the transverse scan points, and N is the number of the 2D image slices, as illustrated in Fig. 5. Both time-domain (TD) and Fourier-domain (FD) OCT have the same three distortions defined above, *i.e.*, spherical distortion, fan-shaped distortion and keystone distortion. The following correction methods are suitable for both TD OCT and FD OCT and there are only some small differences in the processing steps. Demonstration of this method in this paper is based on an SS-OCT system. The distortion correction is done in three steps:

Step 1. Compensate spherical distortion in the depth direction.

Step 2. Correct keystone distortion in the X-Z and Y-Z planes.

Step 3. Correct fan-shaped distortion in the X-Y plane.

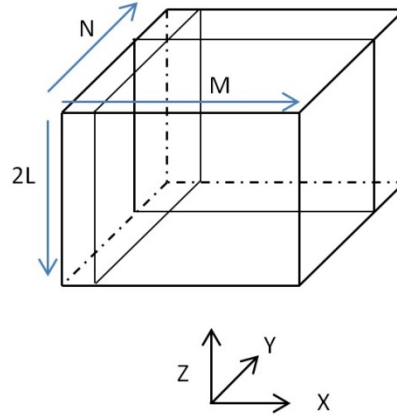


Fig. 5. Matrix data for 3D image reconstruction.

For the spherical distortion, a numerical method has been developed to correct it. When a sample with a flat surface is imaged with an FD-OCT system, the optical path length difference $\Delta Z(\alpha, \beta)$ between the scan angles (α, β) and $(0,0)$, as illustrated in Fig. 2(c), can be calculated using Eq. (1). It should be note that ΔZ is just calculated for scan ray on the surface of sample not include depth in the sample. Then, since FD OCT records the interference signals which are determined by the phase difference between the reflected light signals from the sample arm and reference arm, we can simply subtract the phase corresponding to the optical path difference $\Delta Z(\alpha, \beta)$ to compensate this distortion in depth scan. This can be easily implemented by using the following equation:

$$D_{(l,m,n)}' = D_{(l,m,n)} \cdot \exp(-i \cdot k_l \cdot \Delta Z(\alpha_m, \beta_n)) \quad (4)$$

where $D_{(l,m,n)}$ is a data point in the recorded data matrix depicted in Fig. 4, $D_{(l,m,n)}'$ is the corrected $D_{(l,m,n)}$ data point and k_l is the wavenumber at the l^{th} point of an A-line, α_m is the fast scan angle of the m^{th} A scan line, and β_n is the slow scan angle of the n^{th} B scan frame. The fundamental of Eq. (4) is that the A scan modulation will generate a constant shift in spatial domain after fast Fourier transform (FFT). Radial scan induces additional ΔZ into depth scan, so modulating A scan data and do FFT can correct the spherical distortion in spatial. Equation (4) is applied to all data points for every A-line. Then FFT is performed to all A-line data line by line. At this point, the spherical distortion is corrected. After removing the imaginary part of the data during the image processing, the resultant 3D OCT image contains $L \times M \times N$ pixels. To apply this method in TD OCT, the recorded interferogram data must first be converted into its spectral format by FFT, and then the phase subtraction using Eq. (4) can be executed.

The spherical distortion can be corrected by compensating the phase directly in the interferogram data, but it is more convenient to correct the fan-shaped and keystone distortions in the geometrical space. The correction of these two distortions is performed on the reconstructed 3D OCT images obtained after the spherical distortion compensation is completed. That means the spherical distortion is corrected as the image is acquired while other two distortions need post-image acquisition processing.

First let us look at the keystone distortion. As Fig. 6(a) illustrates, the solid lines represent the actual scanning area of each B scan, i.e., an image slice in the depth direction, and the dotted rectangle is the displayed OCT image without correction. To correct this keystone

distortion, the dotted rectangle must be transformed to the solid-line keystone shape. The method is simply to scale each B scan image slice line by line with a scaling factor given by

$$S_l = \frac{OT_x'(\alpha_{\max}, \beta_n)}{OT_x''(\alpha_{\max}, \beta_n)} \times \frac{L-l}{L-1} + \frac{l-1}{L-1}, l = 1, 2, 3, \dots, L \quad (5)$$

where OT_x' and OT_x'' are respectively the x-components of the vectors \overline{OT}' and \overline{OT}'' , and α_{\max} is the maximum angle of the fast scan. Since the keystone distortion also exists in Y-Z planes, a similar algorithm needs to be applied to complete this distortion correction.

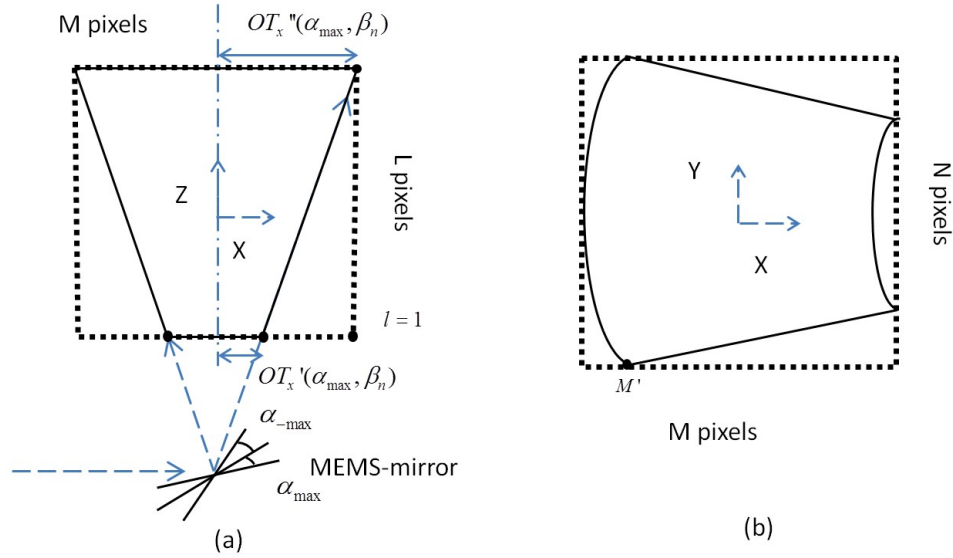


Fig. 6. Digital image process for keystone and fan-shape distortions correction. (a) Keystone distortion corrected by image rows scaling; (b) transverse scan pattern (solid lines) and original display form of OCT images (dotted rectangle).

In order to correct the last fan-shaped distortion, the en-face image in the X-Y plane, i.e., the dotted rectangle in Fig. 6(b), is transformed into the solid-line fan shape by the following processing steps:

Firstly, the n th row of the en-face image is scaled by a factor of S_n , given by Eq. (6), to the right side. β_{\max} is the maximum angle of the slow scan.

$$S_n = \frac{OT_x'(\alpha_{\max}, \beta_n) - OT_x'(\alpha_{\max}, \beta_{\max})}{OT_x'(\alpha_{\max}, \beta_{\max}) - OT_x'(\alpha_{\max}, 0)}, \quad n = 1, 2, 3, \dots, N \quad (6)$$

Secondly, the n th row of the image is shifted to the left by P_n pixels and P_n is given by

$$P_n = \frac{OT_x'(\alpha_{\max}, \beta_{\max}) - OT_x'(\alpha_{\max}, \beta_n)}{OT_x'(\alpha_{\max}, \beta_{\max}) - OT_x'(\alpha_{\max}, 0)} \times M, \quad n = 1, 2, 3, \dots, N \quad (7)$$

Now, the dashed rectangle area is changed into the solid line shape as Fig. 7(a) shows.

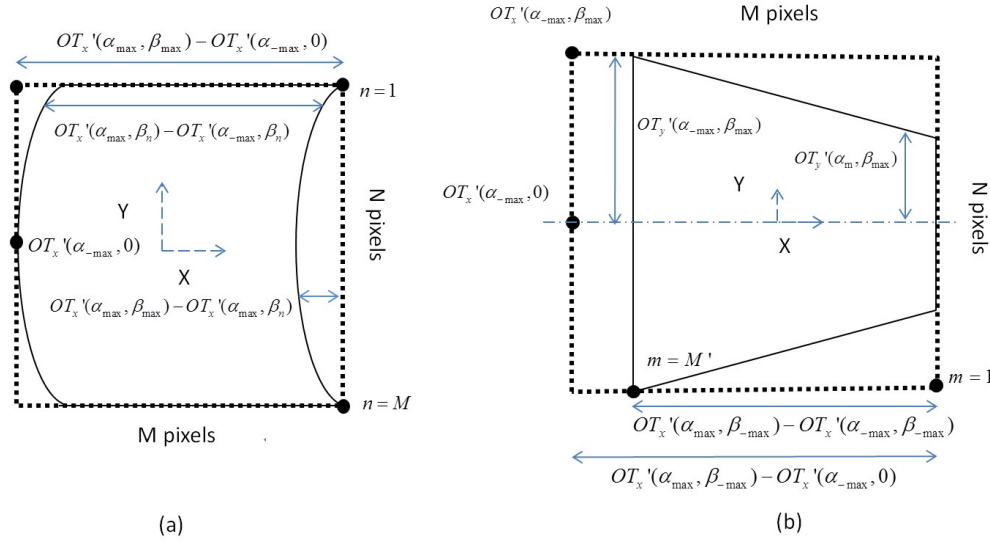


Fig. 7. (a) Solid lines present results of scaling each row to the right side followed by shifting some pixels to the left; and (b) Column by column scaling.

Lastly, each en-face image is scaled down column by column according to the following equation,

$$S_m = \frac{OT'_y(\alpha_m, \beta_{\max})}{OT'_y(\alpha_{-\max}, \beta_{\max})}, \quad m = 1, 2, 3, \dots, M' \quad (8)$$

where OT'_y is the y-component of vector $\overline{OT'}$, and M' is given by Eq. (9) which means not all the M columns need to be transformed and just executed till the M' column pointed in Fig. 6(b). Figure 7(b) illustrates the effect of scaling in columns alone. Then all the en-face images will be free of fan-shaped distortion.

$$M' = \frac{OT'_x(\alpha_{\max}, \beta_{-\max}) - OT'_x(\alpha_{-\max}, \beta_{-\max})}{OT'_x(\alpha_{\max}, \beta_{-\max}) - OT'_x(\alpha_{-\max}, 0)} \times M \quad (9)$$

With these distortions correction efforts, three-dimensional reconstruction of OCT images will be free of scan distortions. C++ is used to program the algorithm. The amount of time of each distortion correction is calculated based on a computer with Pentium dual-core E5800 and 4 GB memory. For spherical distortion, it takes 100ms to execute FFT and image quantization of each image frame. Scaling an image with 608*512 pixels only takes 16ms, which is the time also needed for other two distortions compensation. To implement real time display, 10 threads programming of C++ are opened to reduce each image display interval into 10ms.

3. Experiment and results

A MEMS mirror based endoscopic SS-OCT system described above was established for experimental verification of the proposed method. The swept-source laser (Axsun Tech.) has a center wavelength of about 1310 nm. It sweeps in k-space at 50 kHz and generates a linear K clock sequence for A-scan. The maximum number of K clocks in each sweeping period is 1286, which corresponds to wavelengths from 1260nm to 1360nm. In previous work, only 1024 K points were used and acquiring more spectral data could increase image depth. In our experiment, 1216 K points are selected for each A-scan because it works well for real time display by FFTW3 which is the fastest program to execute FFT [18]. The fast scan rate is set

at 50 Hz and 512 sample points are taken for each A scan. For each B scan, 100 2-D image frames are stored and then reconstructed to form 3D images.

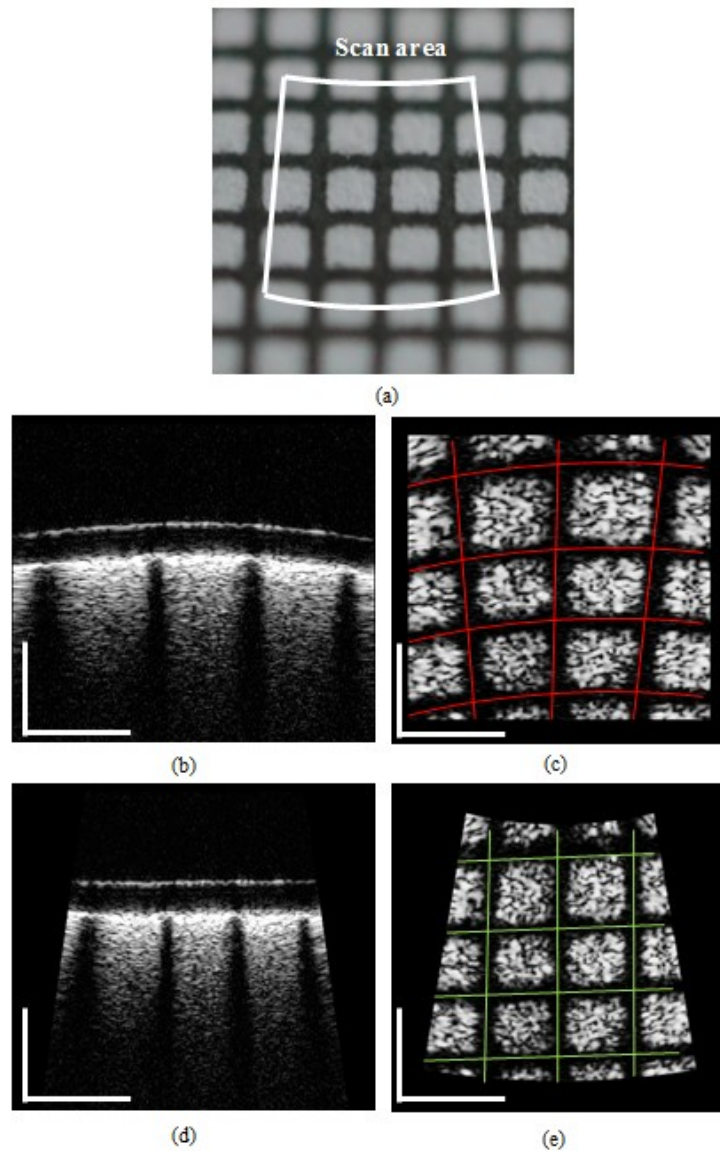


Fig. 8. (a) square array sample; (b) cross section image with spherical distortion; (c) fan-shape distortion in transverse plane; (d) cross section image after distortion corrected; (e) transverse plane after distortion corrected. White scale bar represents 1mm.

The imaging experiment was performed on several samples. Figure 8(a) shows a paper printed with square arrays of $0.8\text{mm} \times 0.8\text{mm}$ covered by a thin glass to ensure its surface flatness. This sample was set 3mm away from the optical window of the probe by a microstage and was imaged using the MEMS-based endoscopic SS-OCT. Figures 8(b) and 8(c) show the OCT images without distortion correction. Flat surface suffers the spherical distortion is obviously seen in a B-scan image shown in Fig. 8(b) cross-section image. Fan-shaped distortion was also observed in an en-face image shown in Fig. 8(c). The maximum distortion is about 25%. To apply the distortion correction algorithms, the output light vector

\overline{OT} is calculated first. The value of the parameter d is 4.8 mm for \overline{OT}' and 9.8mm for \overline{OT}'' . After scan distortions using the correction methods described in section 2, the scanning distortions were greatly suppressed in OCT images, as evidenced in Figs. 8(d) and 8(e). The depth cross-sectional image (Fig. 8(d)) has a flat surface now and retrieves its keystone scan pattern. The fan-shaped distortion was compensated and the original square arrays were also recovered (Fig. 8(e)). After distortion correction, the residual distortions are less than 5%.

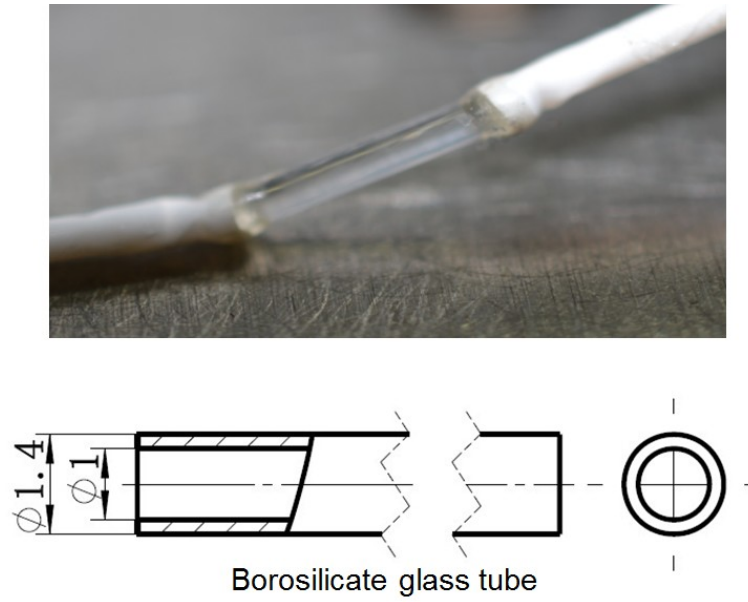


Fig. 9. Glass tube

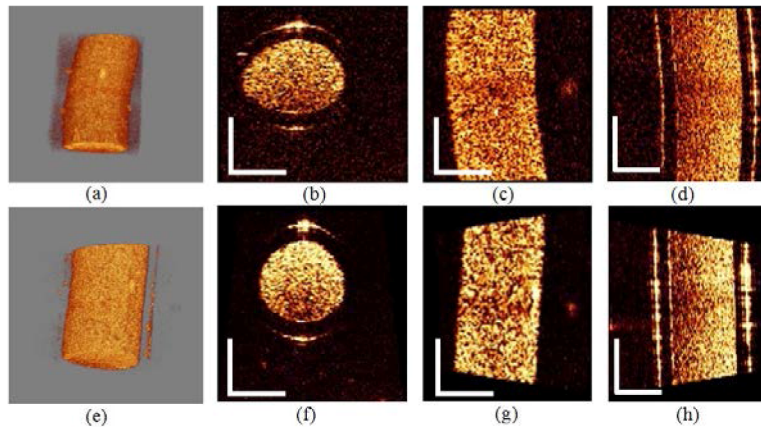


Fig. 10. OCT images of Glass tube filled with milk. (a): 3D structure of original OCT image. (b)-(d): orthographic views with scanning distortion. (e) 3D structure of compensated OCT image. (f)-(h): orthographic views with scanning distortion free. White scale bar represents 1mm.

It should be noted that the proposed methods can deal with samples with arbitrary shapes as well as flat surfaces. For further validation, a glass tube filled with milk fluid was tested. The experiment was based on a commercial milk sample with a 3% fat volume concentration whose reflective index was about 1.35. The milk was injected into a glass tube whose reflective index is 1.51, as shown in Fig. 9. The tube inner diameter is 1mm and outer

diameter is 1.4mm. Figure 10 shows its OCT images before and after distortion correction. Before distortion correction, the straight glass tube appears bent deformation. After correction, both the bending and its contour restored straight line and the transect circles were also recovered from elliptical deformations.

4. Conclusion

The scan patterns and distortions of a two-axis MEMS mirror-based OCT probe are studied. Three types of scan distortions are identified. A numerical method has been developed to compensate the spherical distortion in the phase domain and correct the fan-shaped and keystone distortions by using a series of three-dimensional transformations. Experiment results have verified the effectiveness of the proposed approach in correcting the OCT image distortions generated by a two-axis MEMS scanning mirror.

Acknowledgments

This work is supported in part by the Innovation Fund Project for Graduate Student of Shanghai (JWCXSL1201), the National Basic Research Program of China (2011CB707504) and the US National Science Foundation under award #1002209.